San Jose State University

SJSU ScholarWorks

5-1-2021

Mobile Ka-Band Polarimetric Doppler Radar Observations of Wildfire Smoke Plumes

TAYLOR B. AYDELL
San Jose State University

CRAIG B. CLEMENTS
San Jose State University, craig.clements@sjsu.edu

Follow this and additional works at: https://scholarworks.sjsu.edu/faculty_rsca

Recommended Citation

Mobile Ka-Band Polarimetric Doppler Radar Observations of Wildfire Smoke Plumes

Taylor B. Aydell[a] and Craig B. Clements[a]

[a] *Fire Weather Research Laboratory, Department of Meteorology and Climate Science, San José State University, San José, California*

ABSTRACT: Remote sensing techniques have been used to study and track wildfire smoke plume structure and evolution; however, knowledge gaps remain because of the limited availability of observational datasets aimed at understanding fine-scale fire–atmosphere interactions and plume microphysics. Meteorological radars have been used to investigate the evolution of plume rise in time and space, but highly resolved plume observations are limited. In this study, we present a new mobile millimeter-wave (Ka band) Doppler radar system acquired to sample the fine-scale kinematics and microphysical properties of active wildfire smoke plumes from both wildfires and large prescribed fires. Four field deployments were conducted in autumn of 2019 during two wildfires in California and one prescribed burn in Utah. Radar parameters investigated in this study include reflectivity, radial velocity, Doppler spectrum width, differential reflectivity Z_{DR}, and co-polarized correlation coefficient ρ_{HV}. Observed radar reflectivity ranged between -15 and 20 dBZ in plume, and radial velocity ranged from 0 to $16\,\mathrm{m\,s^{-1}}$. Dual-polarimetric observations revealed that scattering sources within wildfire plumes are primarily nonspherical and oblate-shaped targets as indicated by Z_{DR} values measuring above 0 and ρ_{HV} values below 0.8 within the plume. Doppler spectrum width maxima were located near the updraft core region and were associated with radar reflectivity maxima.

KEYWORDS: Forest fires; Wildfires; Radars/radar observations; Remote sensing

1. Introduction

Wildfires are high-impact societal problems for the western United States and other fire-prone regions that can result in loss of life, property, and natural resources as well as degraded human health through the release of smoke and by-combustion products (Dempsey 2013; McRae et al. 2015; Clements et al. 2018). Wildfires can cause regional- to global-scale impacts through smoke injection into the atmosphere such as reduced solar radiation (Penner et al. 1992; Price et al. 2016), altered aerosol concentrations in the upper and lower atmosphere (Fromm et al. 2006), and unexpected smoke transport (Lareau and Clements 2015). Therefore, there is a need to better understand wildfire plume dynamics and smoke transport; however, progress has been hampered by a lack of near-field plume observations.

The impact of wildfire plume dynamics on fire behavior has long been questioned. Several studies have tried to address processes associated with deep pyroconvection (Rodriguez et al. 2020; McCarthy et al. 2019; Lareau et al. 2018; McRae et al. 2015) and extreme fire behavior, particularly their role in short- and long-range firebrand transport, further complicating the ability to deterministically model fire spread associated with these phenomena (Cruz et al. 2012; McCarthy et al. 2018). Understanding these dynamical processes and their impact on fire behavior is important to develop better predictive tools for fire management.

Wildfire plume microphysics research has used various types of remote sensing platforms that requires an understanding of the returned backscatter, putting an emphasis on resolving the scattering sources and their relationship to the physical properties of wildfires. And while recent progress in wildfire plume microphysics has detailed the larger particles and aerosols that are generated from the combustion processes (Banta et al. 1992; Baum et al. 2015; LaRoche and Lang 2017; Jones and Christopher 2009, 2010; McCarthy et al. 2018, 2019), few observational studies have aimed to address the characteristics of the particles that reside in the submicron range. Previous studies have shown that ash is the dominant scattering source within smoke plumes, revealing the presence of nonspherical and horizontally oriented plume particles (Melnikov et al. 2008, 2009; Lang et al. 2014). Beyond the basic geometry and size distributions of smoke plume particles, knowledge about the dynamic components and electromagnetic properties of scatterers is also limited (McCarthy et al. 2019).

Ground-based active remote sensing, such as meteorological radar and lidar, can address some of the methodological difficulties of observing in the wildland fire environment (Fromm et al. 2012; McCarthy et al. 2018; Clements et al. 2018), particularly when deployed following standard fire safety protocols. For example, scanning Doppler lidar has been used to resolve the dynamics, kinematics, and turbulent properties of wildfires through analysis of lidar backscatter intensity and radial velocity estimates (Banta et al. 1992; Charland and Clements 2013; Lareau and Clements 2016, 2017; Clements et al. 2018). Limitations of using lidar include range (typically < 10 km) and attenuation in moist convection and optically thick plumes with high ash density.

Lidar has been used to study wildfire plumes, but meteorological radar has been used less for wildfire research, with applications primarily in a supplemental capacity (McCarthy et al. 2019). Meteorological radars are capable of employing a range of microwave frequencies to obtain high-resolution,

Corresponding author: Craig B Clements, craig.clements@sjsu.edu

near-real-time data without compromising the safety of those conducting the research. One of the first pioneering studies utilizing radar for studying wildfires and plume characteristics was that of Banta et al. (1992), in which an X-band Doppler radar and Doppler lidar were used to investigate the internal and external environment of a forest fire plume. Recent investigations into wildfire smoke plume microphysics have focused on the dual polarimetric radar signatures through the analysis of radar equivalent reflectivity factor, radial velocity, and correlation coefficient of large ash and pyrogenic particles (Jones and Christopher 2009, 2010; Jones et al. 2009; McCarthy et al. 2018, 2019; Zrnić et al. 2020). The most common types of radar data used for these studies have utilized the operational dual-polarization radars, such as the NEXRAD WSR-88D network. The wavelength of operational radars (~10 cm) allows for the detection of large, ash particles but limits the observations of small-scale processes within the plume and microphysical properties. Motivated by the need for more detailed wildfire plume sampling, a mobile truck-mounted, millimeter-wavelength radar was used to examine the microphysical regimes of wildfire smoke plumes. Millimeter-wavelength radars are ideally suited to study clouds, small hydrometeors in precipitating systems, and ash lofted by wildfires (Bryan et al. 2017). In this study, we present a new mobile millimeter-wave (Ka band) Doppler radar system to sample the fine-scale kinematics and microphysical properties of active wildfire smoke plumes from both wildfires and prescribed fires. This work demonstrates the advantages of utilizing a portable, millimeter-wavelength radar for monitoring and advancing the understanding of wildfire plume dynamics using close-range observations from the fire environment.

2. Background

Studying pyrometeors, or targets of pyrogenic origin, is difficult because of the complex nature of wildfires and the highly irregular scattering materials within the plumes (McCarthy et al. 2019). It is known that the interaction between electromagnetic waves and radar targets depend on the frequency of the radiation and on the size, shape, composition, and distribution of the material within the beam (Rauber and Nesbitt 2018); however, little is known about these properties of wildfire by-products. The basis of studying pyrometeors from particle scattering is based on the Rayleigh and Mie Scattering theories of Mie's solution to Maxwell's equations for the interaction of radiation with a sphere (Rauber and Nesbitt 2018). Under these theories, radar equivalent reflectivity produced from particle-based scattering is dependent on the wavelength of the radar, the radar cross section per unit volume, and the dielectric constant. The underlying equation of meteorological radars for particle-based scattering is based on the critical assumptions that all targets within the radar beam consist entirely of dielectric spheres and that the particles are much smaller than the wavelength of the radar (Rayleigh scattering theory). A third critical assumption is that the reflectivity returned is the water-equivalent reflectivity, or that the dielectric constant K is 0.93. Therefore, in the context of hydrometeors, these factors are known for a wide range of

meteorological phenomena. There have been studies to find a dielectric constant more suited for studying pyrometeors (Adams et al. 1996); however, the derived value of K has not been used to analyze radar reflectivity from wildfires and would not be comparable to any literature.

Geometric properties, those that detail the shape, surface area, and aspect ratio, affect how much energy is returned to the radar. Previous findings indicate that the primary source of scatterers within wildfire plumes are ash particles and are considered to primarily be seen as needlelike by the radar (Banta et al. 1992; Melnikov et al. 2009; Baum et al. 2015). The electromagnetic properties, which are a function of the molecular composition, mass, and temperature, have primarily been studied using laboratory settings and a theoretical framework. Baum et al. (2015) analyzed the electromagnetic material properties of ash particles through the analysis of their complex permittivity. They considered ash to have two modes of dynamic behavior during descent, concluding that radars effectively see pyrometeor targets as horizontally oriented, needle-like structures. The lack of in situ observations of pyrometeor properties has limited the understanding of wildfire targets, therefore constraining the interpretation of wildfire radar signatures and representing a significant gap in our understanding of wildfire plume microphysics.

3. Data and method

a. Radar specifications

The Ka-band Scanning Polarimetric Radar (KASPR) was manufactured by Prosensing, Inc. (ProSensing 2019), and acquired by San José State University to sample fine-scale fire–atmosphere interactions within ash and debris plumes of wildfires. KASPR is a fully scanning, dual-polarimetric millimeter-wavelength radar suited for studying clouds, small hydrometeors, and ash lofted by wildfires. KASPR operates at 35.68 GHz with a solid-state power amplifier that has a peak power of 10 W and an antenna with a diameter of 1.8 m. This unit is composed of a radar transmitter, antenna, elevation and azimuth scanning pedestal, control software, digital receiver, and electronics enclosure. The radar pedestal is mounted to a flatbed deck on a Ford F-250 4 × 4 pickup truck (Fig. 1d). An automatic leveling system (Bigfoot Leveling Systems AC-12K24) levels the truck and radar in under 3 min once arrived on site. This hydraulic leveling system provides 24-in. (1 in. = 2.54 cm) throw and has a 12 000-lb. (1 lb = 0.45 kg) load capacity per jack, providing a safe and stable platform for deployments.

The software of the radar system provides various data processing functions, including pulse compression, clutter filtering, continuously updated noise estimation, FFT processing, and calibrated dBZ computation. For real-time monitoring of the output data, KASPR has a display client that can be operated from the unit or remotely from any location. For operations, the radar specifications are well suited for deployments that observe targets within 15 km of the radar. Range resolutions for the system vary from 7.5 to 120 m; however, it is primarily operated at the 15- and 30-m range
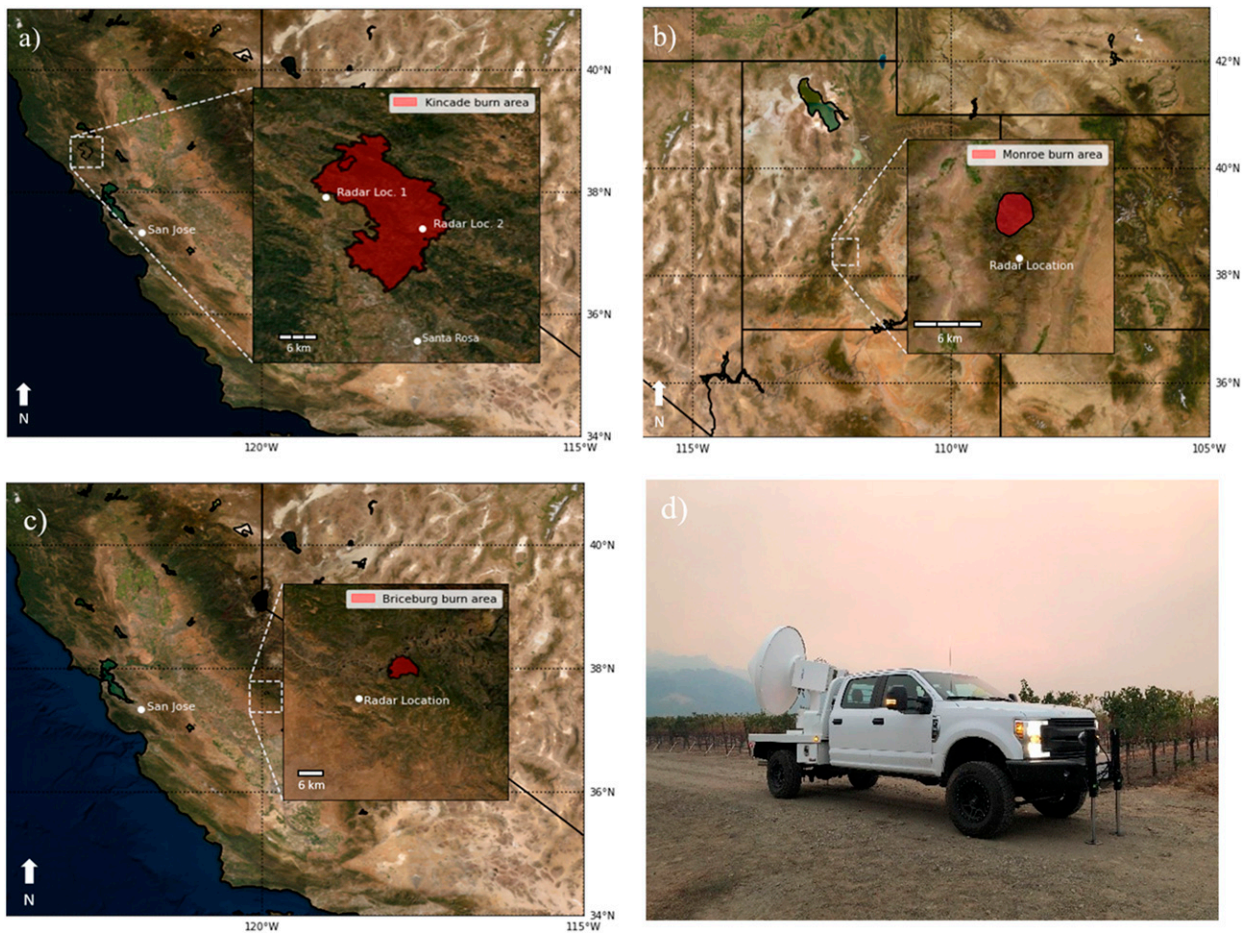
FIG. 1. Maps of the (a) Kincade, (b) South Monroe, and (c) Briceburg fires and the location of the radar site. (d) A photograph of the radar unit that was taken on the first deployment on 23 Oct 2019.

resolution for our plume observations. Additional radar specifications and an overview of the output parameters used in this study are summarized in Table 1.

b. Deployment rationale

The design of our deployable radar unit allows for rapid deployments to fires using the "storm chaser" approach that is widely used in the severe weather community (Bluestein 1999). Our deployment strategy requires all team members to be fire line qualified to ensure the safety of all research members and equipment during operations (Clements et al. 2018). Communication with key fire personnel and fire management agencies was maintained during all operations at wildfires and prescribed fires. Deployment site decisions are largely influenced by the local terrain attributes and ambient meteorological conditions. Sites were chosen on the basis of accessibility and safety while remaining at a distance that satisfies our research objectives.

Four field deployments were conducted in autumn of 2019 during two wildfires in California and one prescribed burn in Utah. Figures 1a–c illustrate maps of the total burned area from each of the wildfires and the location of the radar. The

Briceburg fire in Mariposa County, California, began on 6 October 2019 and was the first wildfire to which we deployed the radar (Fig. 1c). The second and third deployment were to the Kincade wildfire in Sonoma County, California, which was active from 23 October to 6 November 2019 (Fig. 1a). Last, we collected data on a large, prescribed crown fire (a high-intensity fire burning the forest canopy) as part of a multi-agency field campaign in Fishlake National Forest, Utah, on 7 November 2019 (Fig. 1b). Apart from the Briceburg wildfire, all observations were made from within 5 km of the active fire front. Briceburg observations were taken from 12 km southeast of the fire, and therefore the resolution of this dataset is lower than the others. Additional details for each fire and deployment specifications are listed in Table 2.

c. Scanning procedures

Various scan procedures can be used to study the structure and evolution of debris and ash plumes (Jones and Christopher 2009, 2010; Melnikov et al. 2008; McCarthy et al. 2018). Scan procedures were not decided prior to deployment, but rather on a case-by-case basis that depended on the environmental conditions and direction from which the scans were taken.

TABLE 1. KASPR specifications and operating characteristics.

Parameter	Specification
Frequency	35.68 GHz (wavelength 8.4 mm)
Transmitter power	10-W peak SSPA, 25% duty cycle max
Antenna diameter	1.82 m
Antenna polarization	Transmit: alternate H/V polarization; receive: simultaneous V/H polarization
Beamwidth	0.31°
Low-noise amplifier noise figure	2.8 dB
Range resolution	7.5, 15, 30, 60, and 120 m
Max scan rate	20° s^{-1}
Radar data products	dBZ_V, dBZ_H, L_{DR}, Z_{DR}, ρ_{hv}, and Φ_{DP} power spectra: VV, HH, HV, HH; velocity and spectral width; dual pulse repetition interval velocity for alias unwrapping

In this study, two types of scanning techniques were used: range–height indicator (RHI) and plan position indicator (PPI). RHI scans were used to obtain vertical cross sections through the plume to detail the vertical distribution of various radar variables. Low-elevation PPI scans were performed to collect horizontal cross sections of the near-fire atmosphere. Depending on the fire's location, various azimuth and elevation angles were used to optimize the observations of the plume. The specific scanning routines used at each fire will be discussed in the analyses section and are listed in Table 2.

d. Noise and clutter

Four datasets in total were analyzed in this study, with five types of radar data represented. All data analyses conducted were completed using the open-source PyArt package (Helmus and Collis 2016). Several efforts were made to mitigate ground clutter and the effects of noise sources on the output variables. Various gate filter thresholds were used to mitigate these effects through the PyArt package. The first gate filter applied excluded masked and invalid returns to the radar for all variables. Further inspection of the scans revealed a significant amount of clutter around the smoke plume boundaries, therefore additional gate filters were applied to specific parameters where noise artifacts were present. Radial velocity returns with values between −1 and 1 m s^{-1} were excluded from the analysis. The maximum in plume radial velocity was measured at 28.6 m s^{-1}; therefore, values greater than ±30 m s^{-1} were also excluded. Additionally, the copolar correlation coefficient was also constrained to be within 0.05 and 1.0. Values outside this threshold would not be representative of the smoke plume or any meteorological target. With these thresholds in place, a significant reduction in

noise was achieved. Last, specific differential phase (K_{DP}) calculations were made through the PyArt package following the estimation schemes by Maesaka et al. (2012), Schneebeli et al. (2014), and Vulpiani et al. (2012).

The following analyses will address the characteristics of radar reflectivity, velocity, and the polarimetric variables to detail the radar specific signatures of the ash and debris plumes sampled. First, the datasets collected from the Kincade wildfire deployments are examined. These data detail the evolution of the plume during a period where both RHI and PPI scans were made. Following this analysis, RHI scans made of the vertical plume growth during the South Monroe prescribed burn are examined. Last, the Briceburg wildfire radar reflectivity and velocity signatures are discussed.

4. Kincade wildfire observations

The Kincade wildfire ignited on 23 October 2019 at approximately 38.769°N, 122.767°W in Sonoma County, California (Cal Fire 2019b). This wildfire was the largest wildfire of 2019 in the United States, caused the evacuation of ~190 000 people, and burned a total of 77 758 acres (1 acre = 0.4 ha) (Cal Fire 2019b). For comparison, the Camp fire in 2018 burned a total of 153 336 acres and stands as the deadliest wildfire in California's history (Cal Fire 2019c). Two deployments were conducted during this wildfire and will be denoted as D1 and D2 hereinafter. Deployments were conducted on the first night of ignition, 23 and 24 October, and during a second downslope wind event on 27–28 October. The radar scanned from positions less than 5 km from the active fire fronts. Scanning procedures used for these observations were chosen after assessing the ambient atmosphere conditions and

TABLE 2. Fire and deployment information, including radar scan details.

Fire name	Date of ignition	Date deployed	Lat, lon (°)	Total acres burned	Radar scan strategy	Radar azimuth angle (°)	Corrected azimuth angle (°)
Kincade	23 Oct 2019	23 Oct 2019; 27 Oct 2019	38.972 458, −122.780 053	77 758	D1: RHI; D2: PPI	190°	35°
South Monroe	7 Nov 2019	7 Nov 2019	38.262 00, −112.023 75	~800	RHI	152°	321°
Briceburg	6 Oct 2019	9 Oct 2019	37.604 638, −119.966 06	5563	RHI	82°	47°

local terrain features. Two types of scans, RHI and PPI, were used during D1 and D2, respectively.

a. D1 reflectivity analysis

KASPR was deployed on the night of 23 October 2019 to Alexander Valley (38.945°N, 122.705°W) in Sonoma County. At this time, a fire weather watch was in effect for the region with forecast local gusts exceeding $27 \, \mathrm{m \, s^{-1}}$ and poor humidity recoveries in the surrounding mountains in the Sonoma County region. The Kincade wildfire was first reported at 2124 PST during the extreme wind event, rapidly growing to 10 000 acres within the first 6 h after ignition (Cal Fire 2019b). Observations were conducted through the night of 23 October and into the following morning.

To examine the radar signatures of the Kincade wildfire plume, we analyzed radar reflectivity factor, Doppler velocity, and dual-polarimetric parameters. Figures 2a–h show radar reflectivity and velocity during the early morning of 24 October. The chosen scanning procedure for this time was an RHI scan that captured the vertical propagation of debris above the active fire front and the dispersion of lofted smoke and ash. Our target elevation angles were 5°–160° at an azimuth angle of 35° (Table 2). The target scan rate was at $4° \, \mathrm{s^{-1}}$. The smoke plume remained below 3 km AGL, with few return signals above this level. The active fire-front region was located on a ridge; therefore, elevation scans below 5° were not made.

Figures 2a–h illustrates the evolution of radar reflectivity and Doppler velocity during the first night of fire spread. Specifically, these scans detail a 4-min segment during which the smoke plume propagated vertically and advected downwind. Radar reflectivity values ranged from −20 to 15 dBZ in the plume, with the highest returns corresponding to the area above the active fire front located 5.8 km upwind. During this scan time, ash and debris were observed falling out of the plume onto the radar deployment site, resulting in reflectivity returns just above the scan location. Above the radar location, reflectivity returns ranged from −10 to 0 dBZ, illustrating that smaller particles remained lofted above the surface. In general, the maximum reflectivity values were confined closer to the fire-front region, while smaller pyrometeors were advected downwind and eventually fell out. A notable feature within the reflectivity data is the location of weak returns directly underneath the plume base. This region of weak reflectivity was associated with values between −14 and −8 dBZ (~4 km upwind) and likely represents the fallout of small debris and ash particles ahead of the plume as a result of clean-air entrainment. With time, this area of weak reflectivity extended vertically and increased in magnitude as the plume grew vertically, indicating increased fallout of the smaller particles.

b. D1 Doppler velocity analysis

Analysis of Doppler velocities indicated that plume particles were traveling at 4–$12 \, \mathrm{m \, s^{-1}}$ toward the radar, with some velocities exceeding $15 \, \mathrm{m \, s^{-1}}$ (Figs. 2e–h). The locations of maximum velocities correspond to the maximum radar reflectivity returns above the base of the plume. Observed radial velocities are greatest near the surface and generally weakened

with height, likely as a result of the vertical wind structure associated with the downslope windstorm. At approximately 3 km upwind of the radar location, the scans captured an increase in outbound velocities (red) of magnitude 1–$4 \, \mathrm{m \, s^{-1}}$, indicating horizontal acceleration of the wind toward the base of the plume (~5 km upwind). In contrast, an increase of inbound velocities can be seen to be located downwind of the plume base, at approximately 4 km upwind of the radar. This small region of outbound and inbound velocities indicates the formation of a horizonal convergence zone ahead of the base of the plume. The development of convergence zones downwind of fire fronts has been reported in previous case studies (Clements el al. 2007; Charland and Clements 2013) and is likely driven by the formation of fire-induced circulations.

Acceleration into the upwind side of the plume base (~5.5 km), likely fire induced, is observed for all scan times. Increased velocities near the fire-front location (~5.0 km) likely occurred as a result of a decrease in surface pressure induced by the fire. Underneath this region of increased velocities, an area of clean air is observed to be present in both the reflectivity and velocity data (~4.0 km). This feature is likely indicative of an inflow jet supplying the fire with clean, debris-free air or represents a leeward rotor-like circulation forming downwind of a ridgeline. Because we were scanning perpendicular to a ridge, the elevation could not be lowered to obtain the kinematic structure directly beneath the plume. Along-beam velocities indicate ash and debris were subsiding directly downwind of the radar likely as ashfall. Furthermore, a decrease in radar reflectivity with altitude also suggests that some of the debris may have advected out of the scan plan of the radar.

c. D1 analysis of polarimetric variables

Dual polarimetric observations were collected during the Kincade deployment to detail the microphysical properties of wildfire pyrometeors. Figures 3a–l illustrates the differential reflectivity, correlation coefficient, and Doppler spectrum width for the same period as Fig. 2. Differential reflectivity provides information about the orientation of the scatterers and has been used extensively to detail ash and fire debris lofted from wildfires (Jones and Christopher 2009; McCarthy et al. 2018; Zrnić et al. 2020). As shown in Figs. 3a–d, differential reflectivity (Z_{DR}) returns from this smoke plume are positive and indicate that the targets primarily lie in their horizontal plane. Near the plume base, Z_{DR} values are very inhomogeneous and range from 1 to 6 dB. The locations at which reflectivity returns were the greatest (>5 dBZ), differential reflectivity values were low (0–1 dB). Low Z_{DR} values in areas with high radar reflectivity are likely caused by turbulent and fluttering motions. Conversely, regions with lower reflectivity values were collocated with higher differential reflectivity of values 3–5 dB or where the targets lie in their horizontal plane.

Copolar correlation coefficient (ρ_{HV}) is a parameter that details the statistical consistency of the phase measurements in the radar volume (Rauber and Nesbitt 2018). Copolar correlation coefficient values were low closest to the plume base and ranged between 0.3 and 0.5, indicating that a wide array of
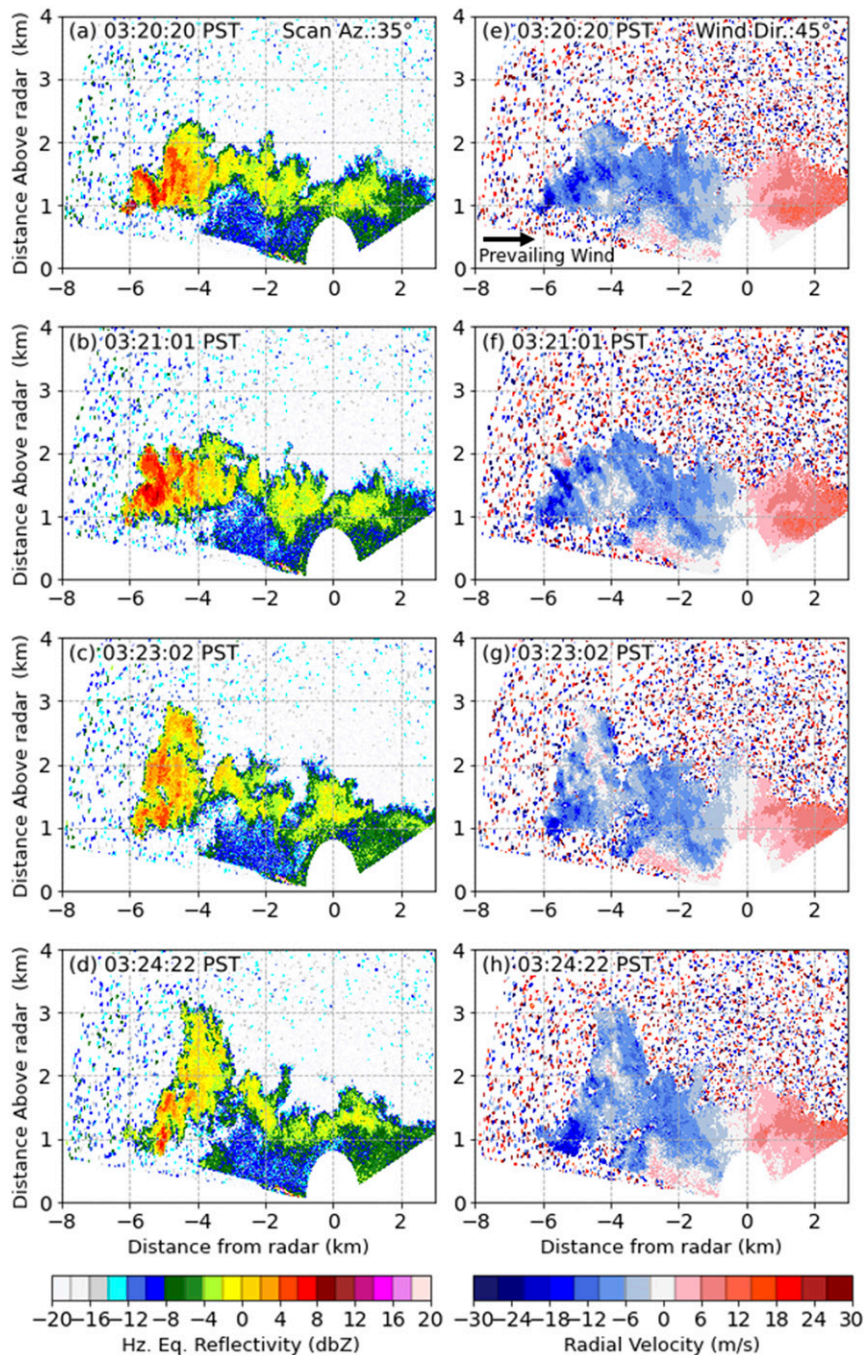
FIG. 2. KASPR radar signatures from D1 to the Kincade wildfire on 24 Oct 2019, showing fields for (a)–(d) horizontal equivalent reflectivity factor (dBZ_H) and (e)–(h) radial velocity (m s^{-1}) beginning at 1520 PST. Scans were taken along the same azimuth for all time periods.

particle shape and sizes with random motions were observed. A slight increase in correlation coefficient with time was observed above the base of the plume (~5 km; Figs. 3f,g). Directly underneath the plume base, near the clean-air region (~4 km), the correlation coefficient varied between 0.7 and 0.8 revealing a more uniform region of the plume. Furthermore, increased values are also observed above the radar site in all

scans presented. Larger correlation values indicate that the more homogenous particles remain lofted in the plume.

Doppler spectrum width is the measure of the spread of radial motions of scatterers within the pulse volume and is primarily affected by wind shear, turbulence, and variations in particle fall velocities. Spectrum width has received little attention for wildfire studies, yet it is an effective tool for
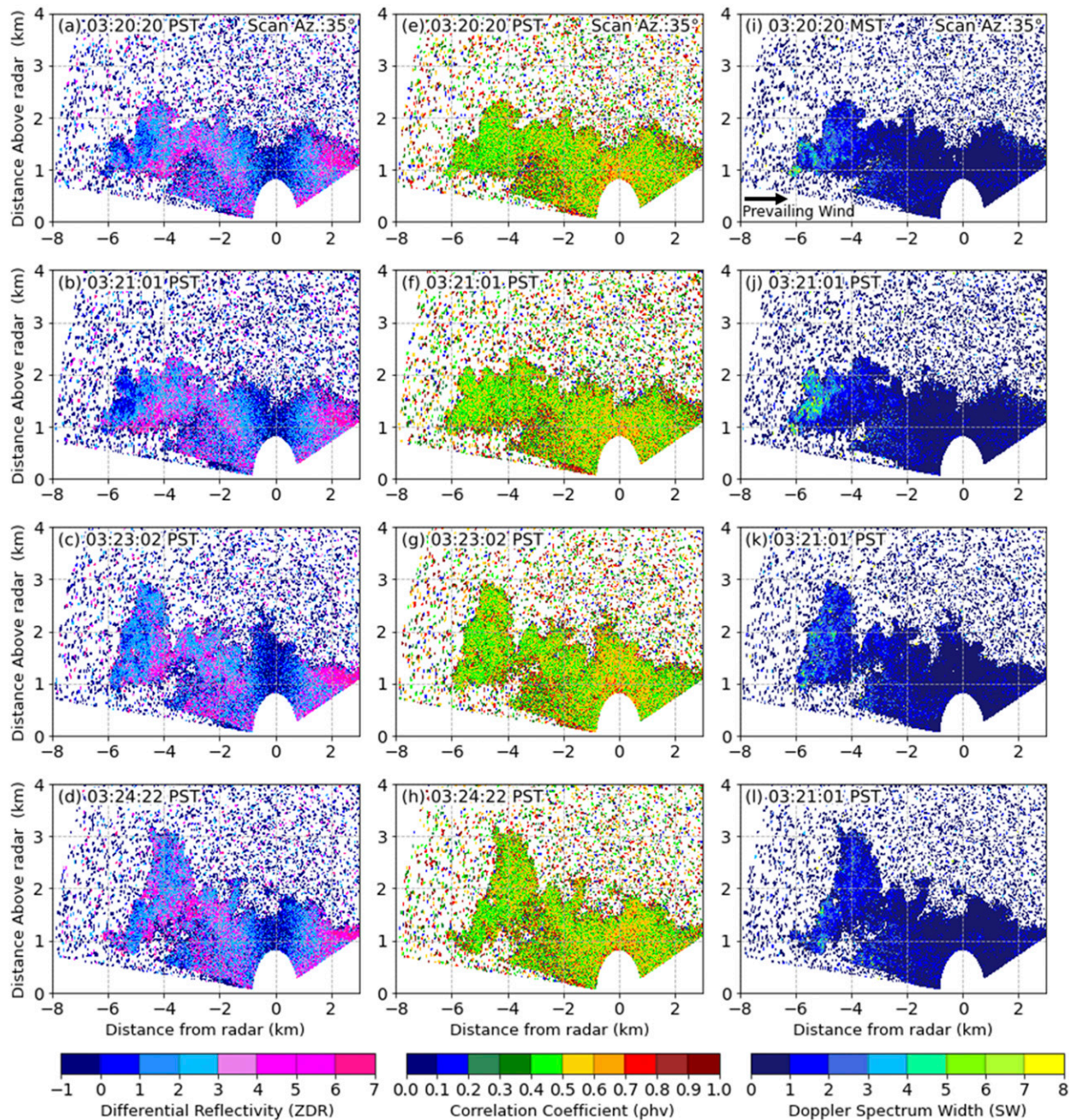
FIG. 3. Same RHI scan as Fig. 2 beginning at 1520 PST 24 Oct 2019, showing fields for (a)–(d) differential reflectivity (Z_{DR}), (e)–(h) copolar correlation coefficient (ρ_{hv}), and (i)–(l) Doppler spectrum width.

highlighting turbulent flow in wildfire convective plumes. The signature of spectrum width highlights consistently low values within the downwind regions of the plume (Figs. 3i–l). Near the updraft zone, where the movement of air is the greatest, regions of higher spectrum width (~5.8 km) indicate the turbulent structure of the plume core (7 m s^{-1}) associated with strong updrafts. Increased spectrum width on the windward side of the plume is also indicative of increased wind shear in this zone. This finding suggests that the updraft cores are the

most turbulent region of the plume. It is also important to note that areas of increased spectrum width correspond to areas where reflectivity and velocity are the greatest. In regions where subsidence increased and the plume is bent over, Doppler spectrum width decreased drastically. The implication of this is that regions where the plume is vertically upright and the updraft intensity is likely the greatest, an increase in Doppler spectrum width should be observed. Understanding the turbulent structures that govern the transport of fire
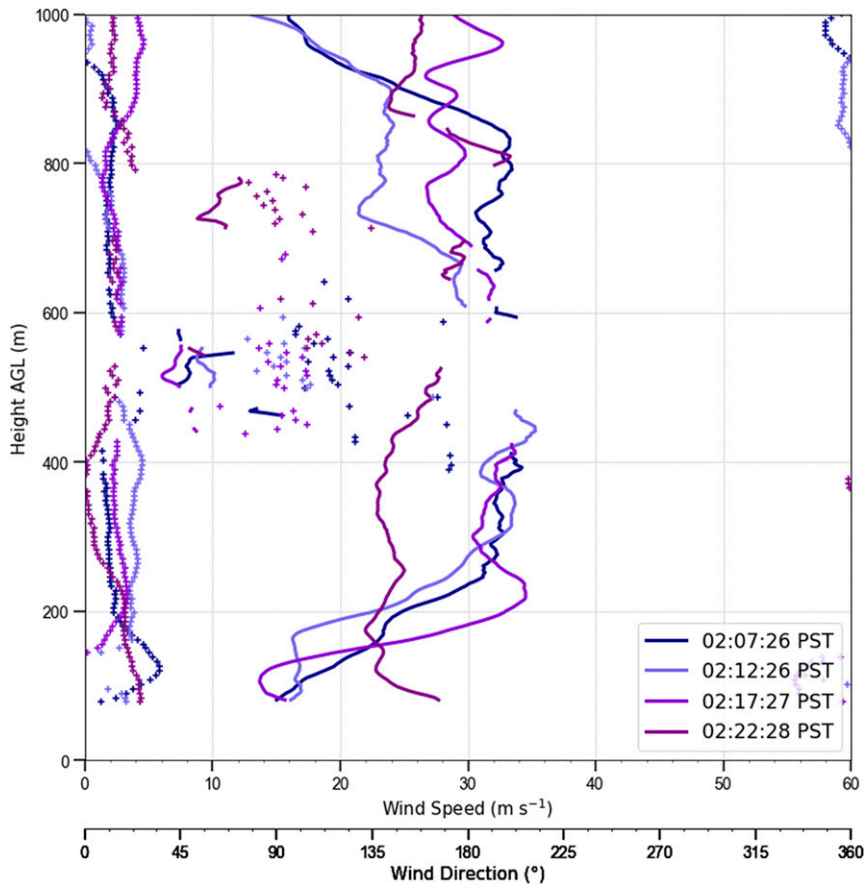
FIG. 4. Doppler lidar vertical wind profiles measured during Kincade D2.

by-products such as firebrands, is highly desirable for validating the turbulent processes of wildfire spread (Koo et al. 2010).

d. D2 reflectivity analysis

KASPR was deployed for a second time to the Kincade wildfire on the evening of 27 October. At this time, a much stronger downslope wind event was forecast to occur during the evening and persist through the early morning. This wind event presented favorable conditions for rapid fire growth and extreme rate of spread. Because this event was forecast days in advance, our secondary profiling truck was also deployed. The California State University–Mobile Atmosphere Profiling System (CSU-MAPS) is equipped with a scanning Doppler lidar and a surface weather station (Clements and Oliphant 2014). These data will not be discussed in detail for this analysis; however, vertical wind profiles are shown to provide context and the ambient wind conditions at the time of KASPR scans. For this deployment, we set up in a vineyard in Knights Valley that was located 5 km from the fire front, allowing for close-range observations of the smoke plume. The deployment site was located perpendicular to the estimated fire spread, providing a safe location from which to scan and with a clear and safe exit route in case the fire moved into the valley.

PPI scans at an elevation angle of 5.04° were used to observe plume structures and evolution through the collection of radar reflectivity, velocity, and Doppler spectrum width (Figs. 5a–l). Vertical wind profiles taken with the Doppler lidar are shown in Fig. 4. At the time of the PPI scans, surface wind speeds measured $15\,\mathrm{m\,s^{-1}}$ out of the northeast. Aloft, wind speeds increased to a maximum of $34\,\mathrm{m\,s^{-1}}$ and remained primarily out of the northeast. Similar to the first deployment, strong ambient wind conditions limited the vertical extent of the plume. Radar reflectivity values were of similar magnitude to that of the first deployment, ranging from -15 to 15 dBZ (Figs. 5a–d). Regions of maximum reflectivity returns were confined to the region of the active fire front and areas associated with isolated updraft cores. Along the edges of the smoke plume, much lower reflectivity values were observed as the debris and ash dispersed laterally. The reflectivity along the edges of the smoke plume increased in area with time. These returns are likely a result of increased debris and ash production from the intensification of the fire front. It is important to note that the feature of increased reflectivity to the north of the fire front is an artifact of the beam hitting a mountain ridge. This feature is only depicted in the last two scans (Figs. 5c,d), as the range of azimuth angles were increased to optimize observations.

e. D2 Doppler velocity analysis

To analyze radial velocity from the radar, it is ideal for the along-beam radial to be aligned with the mean ambient wind.
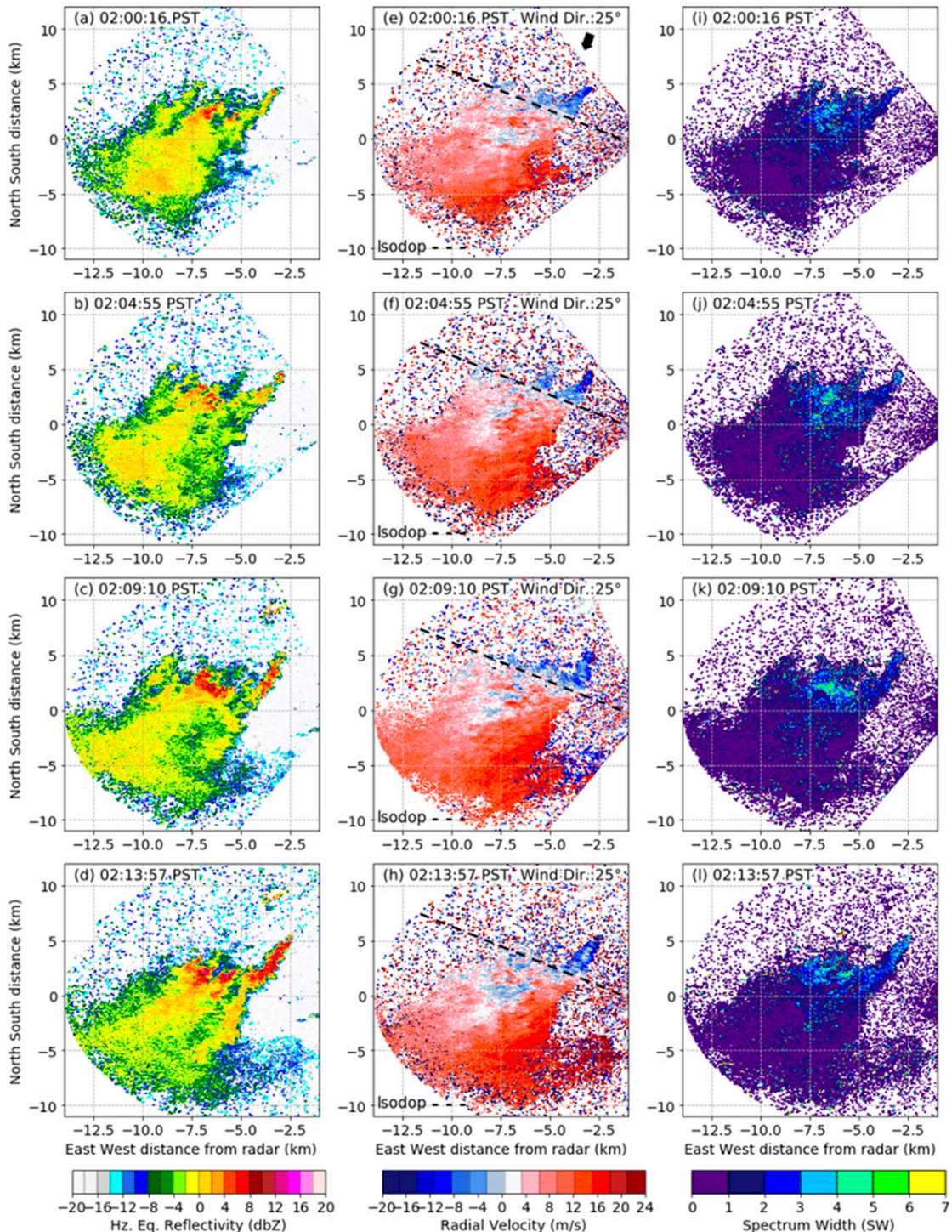
FIG. 5. PPI scans at elevation angle 5.04° at 1400 PST 28 Oct 2019. Signatures from D2 are of (a)–(e) horizontal equivalent reflectivity factor (dBZ_H), (e)–(h) radial velocity (m s^{-1}), and (i)–(l) Doppler spectrum width (SW).

As discussed above, the radar was positioned roughly 5 km to the east of the fire front (Fig. 1a) and almost perpendicular with the direction of the fire, therefore radial velocities are expected to be underestimated from these scans (Figs. 5e–h). Velocity returns indicated the plume was traveling west at 4–15 m s^{-1}; however, we know the plume was strongly influenced by the northeasterly winds present at this time. The strong winds acted to increase fire intensity and aided in carrying debris

downwind, which is observed to extend over 6 km downwind from the fire front (areas of highest reflectivity). At the fire front, inbound velocities were measured to be approximately $8–12\,\mathrm{m\,s^{-1}}$.

f. D2 spectrum width analysis

The Doppler spectrum width reveals the highly turbulent regions within the smoke plume. Values were of similar magnitude as that of the first deployment, ranging from 0 to $7\,\mathrm{m\,s^{-1}}$. Maximum spectrum width values ($7\,\mathrm{m\,s^{-1}}$) were confined to the areas where maximum reflectivities and radial velocities were also observed. On the downwind side of the plume where maximum reflectivity was near 0 dBZ, a sharp decrease in Doppler spectrum width was also observed. Along the plume edge where reflectivity and velocity returns were weak, localized maxima ($\sim5\,\mathrm{m\,s^{-1}}$) in the spectrum width were observed (Figs. 5k,l). These peaks are likely due to increased wind shear and debris transport on the downwind side of the plume and fire front.

5. South Monroe prescribed burn observations

The Fire and Smoke Model Evaluation Experiment (FASMEE) is a collaborative field campaign that aims to identify how fuels, fire behavior, and meteorological conditions interact so that such knowledge can be used to advance operational fire and smoke models (Prichard et al. 2019). To date, this experiment has consisted of two large, prescribed crown fires in Fishlake National Forest, Utah, as a part of the Monroe Mountain Aspen Ecosystem Restoration Project. Prescribed fires are a form of land management in which a planned fire is intentionally set to vegetation. For this study, a prescribed crown fire was used to satisfy the research objectives of the FASMEE campaign and aid in aspen restoration. Radar observations were collected on a stand-replacement fire in mixed-conifer and aspen forest. Several research groups deployed other sensors such as fire behavior packages and fuel measurements to detail the characteristics of the prescribed crown fire.

The Monroe South prescribed fire was ignited on the morning of 7 November 2019. Once completed, this prescribed fire burned a total of approximately 800 acres and produced a visible pyrocumulus that reached ~8.7 km MSL. Our research team deployed to a location 3 km southeast of the burn unit (Fig. 1b). The CSU-MAPS Doppler lidar was used to obtain vertical wind profiles on the morning of ignition. Winds were northeasterly throughout the profile, with speeds measuring $2–4\,\mathrm{m\,s^{-1}}$ near the surface and below $10\,\mathrm{m\,s^{-1}}$ aloft (Fig. 6). Radar observations were collected from 1300 to 1600 MST or the time at which ignitions were conducted. Here we examine the smoke plume evolution of the South Monroe prescribed burn through radar analysis of reflectivity, velocity, and polarimetric parameters beginning at 1300 MST.

a. Reflectivity observations from the South Monroe burn

Various scan procedures were used to detail the plume evolution throughout the day. The focus of this analysis

examines a 1-h period of the smoke plume evolution using an RHI scan procedure (Figs. 7a–h). We had a target scan rate of $8°\,\mathrm{s^{-1}}$ through elevation angles from 3° to 80° (Table 2). Several "puff" structures within the plume were visible after ignition; therefore, scans were chosen to capture the rapid evolution of one of these primary features. Vertical slices through the plume illustrate the distribution and magnitude of reflectivity along the radar beam. Light winds provided a favorable atmosphere for the plume to rise vertically to 6 km AGL during this 1-h period. In addition, a stable layer was observed in the reflectivity data at approximately 2 km AGL and persisted throughout the day. Observed values of reflectivity were between −12 and 20 dBZ within the plume (Figs. 7a–d). In the first scan (Fig. 7a; 1300 MST), maximum reflectivities were confined to the base of the plume where larger, heavier debris was likely located. As the convection column intensified, larger debris was observed to propagate vertically throughout the column (Figs. 7b,c). Low reflectivity values along the stable layer and edges of the smoke plume persisted for all scans. In areas where reflectivity decreased in magnitude between scans (Fig. 7d), particle fallout was likely occurring as ash and debris dispersed aloft.

b. Velocity observations from the South Monroe burn

Vertical slices through the smoke plume allowed for observations of the kinematic structures of the smoke plume and surrounding areas to be measured. In the early phase of the plume rise (Fig. 7e), velocity returns were weak within the plume and values were $\pm6\,\mathrm{m\,s^{-1}}$ to and from the radar. As the fire intensified and the plume extended farther vertically, greater velocities ($\sim25\,\mathrm{m\,s^{-1}}$) were measured 2–4 km above the plume base (Fig. 7g).

Velocity maxima were measured along the center axis of the plume core and likely indicate the location of the updraft core. The edges of the plume are illustrated by much lower measured velocities and weaker returns. Near the base of the plume (Figs. 7e,f), contrasting inbound and outbound velocities indicate a zone of localized convergence. In contrast, the top of the plume is depicted by diverging velocities or divergence aloft for all scans. Above the stable layer on the leeward side of the plume, an area of inbound velocities was observed at 3 km AGL (Figs. 7g,h). This region of inbound velocities proceeded areas of low reflectivity, likely indicating the plume was entraining clean air. In the last scan (Fig. 7h; 1348 MST), inbound velocities decreased and were associated with a decrease in reflectivity of ~8 dBZ. This feature is indicative of clean-air entrainment and ash-particle fallout.

c. Polarimetric observations from the South Monroe burn

Differential reflectivity, correlation coefficient, and Doppler spectrum width signatures of the South Monroe plume are shown in Figs. 8a–l. Differential reflectivities were positive within the smoke plume, although the distribution was highly variable. Similar to the observations of the Kincade wildfire, the updraft zone and regions where reflectivity values are positive are characterized by Z_{DR} values of 0–3 dB. Outside these regions, differential reflectivity values were higher (>3 dB), indicating horizontally oriented targets.
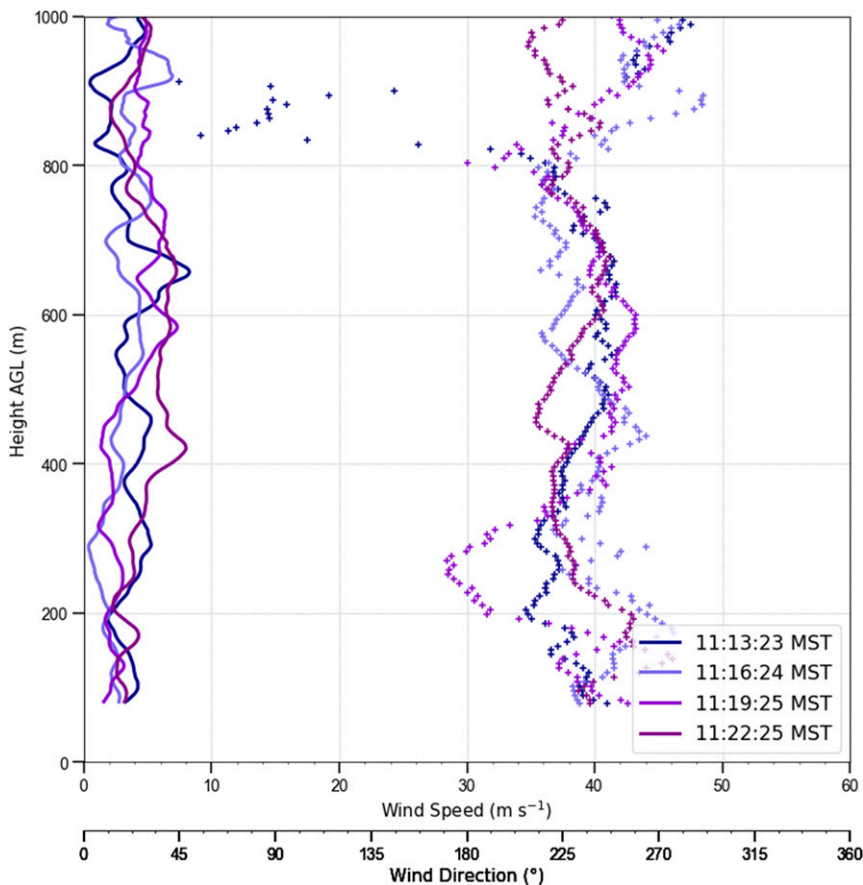
FIG. 6. Doppler lidar vertical wind profiles measured during the South Monroe prescribed burn.

Copolar correlation is highly variable in the plume and no distinct patterns are evident. The magnitude of correlation coefficient values within the plume remained above 0.3 and below 0.8. On the downwind edges of the plume, increased correlation coefficient values were observed. When compared against the correlation coefficient returns from the Kincade deployments, values are a magnitude higher for the South Monroe burn. While this fire did produce a visible pyrocumulus, no signature in the correlation coefficient indicates this process. A shift to larger correlation coefficients would be expected if liquid water was present, yet values remained below 0.8 for all scans. It is likely that the cloud droplets were too small to be measured by the radar because of the chosen scanning parameters. Operating in polarimetric pulse pair mode and scanning at a fast rate lowers the sensitivity of the radar. With this chosen scanning method, we were likely only seeing particles above 100-μm-diameter size, therefore it did not allow for the observation of water droplets. Slightly higher values are observed in the last scan (Fig. 8h) above 3 km; however, returns are highly variable and do not reveal a strong signature of liquid presence. One possible explanation for similar ρ_{HV} values observed through the depth of the plume is that the plume is likely populated with pyrometeors through its entire depth and while the radar does not determine the cloud

base as observed visually, the continuous ρ_{HV} indicates that the pyrometeors extend all the way to the top of the plume and within the observed pyrocumulus.

The Doppler spectrum width returns revealed that the most turbulent and highly variable areas within the smoke plume are located in the central updraft core (Figs. 8i–l). Spectrum width values were of similar magnitude to that of the Kincade wildfire, with values ranging from 0 to 6 m s^{-1}. Spectrum width values were the lowest during the first scan, with the maximum value being 5 m s^{-1} in the updraft core zone (Fig. 6, 3 km). As the fire intensified and the plume increased in size, Doppler spectrum width increased with each subsequent scan likely caused by increased updraft velocities associated with the updraft core. Spectrum width maxima remained confined to the updraft core region located within the central part of the plume while the minimum values persisted along the edges of the plume. In the last scan (Fig. 8l), increased values are observed aloft, at approximately 5 km AGL. The increase in spectrum width at this level is likely a result of increased overturning of the plume and could be caused by wind shear aloft.

d. Mean variables from the South Monroe fire

Figure 9 shows the mean value of each variable along three different elevation angles for the 1-h period. Averaging each of
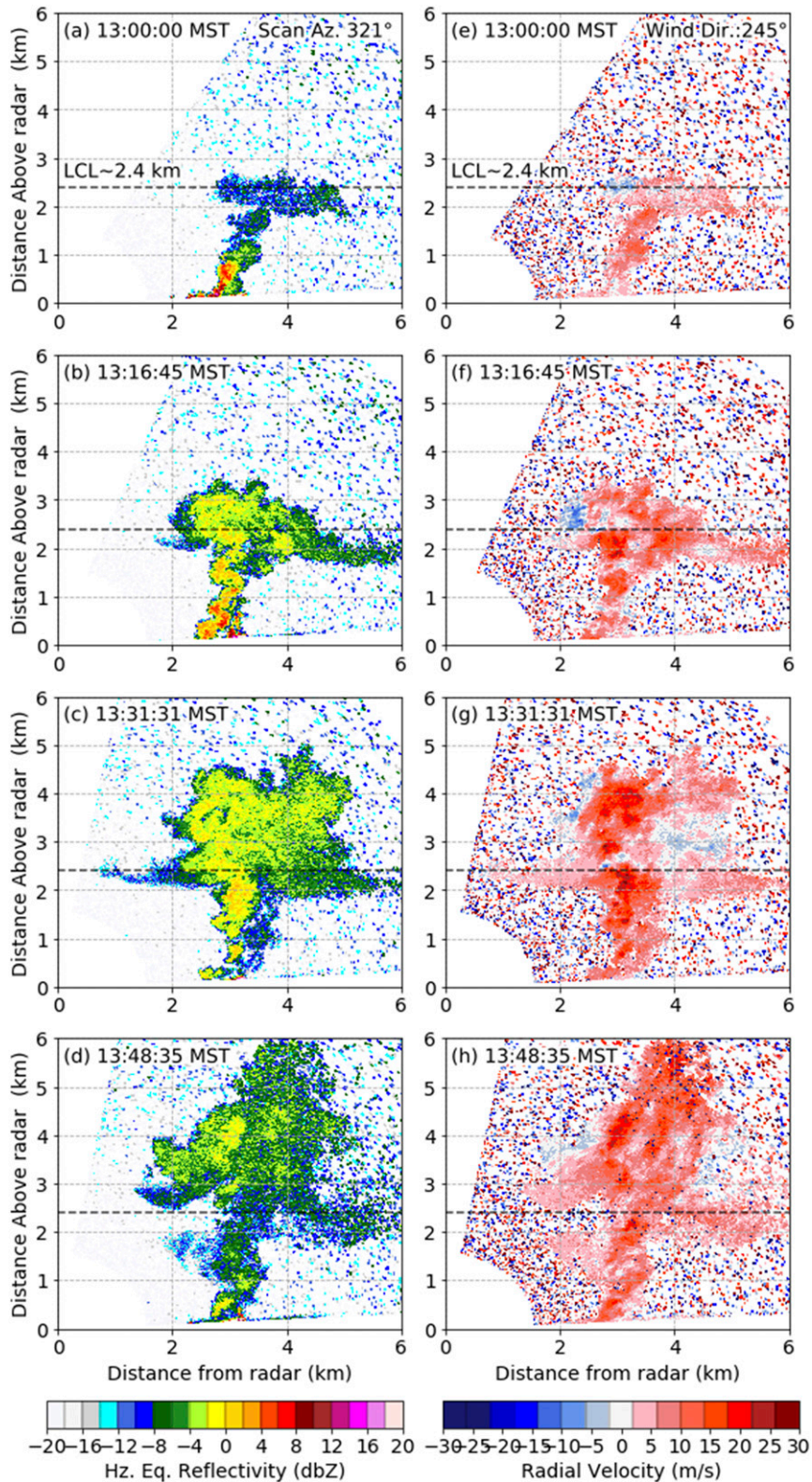
Fig. 7. KASPR radar signatures from the South Monroe prescribed burn of (a)–(d) horizontal equivalent reflectivity factor (dBZ_H) and (e)–(h) radial velocity (m s^{-1}) beginning at 1300 MST 7 Nov 2019.
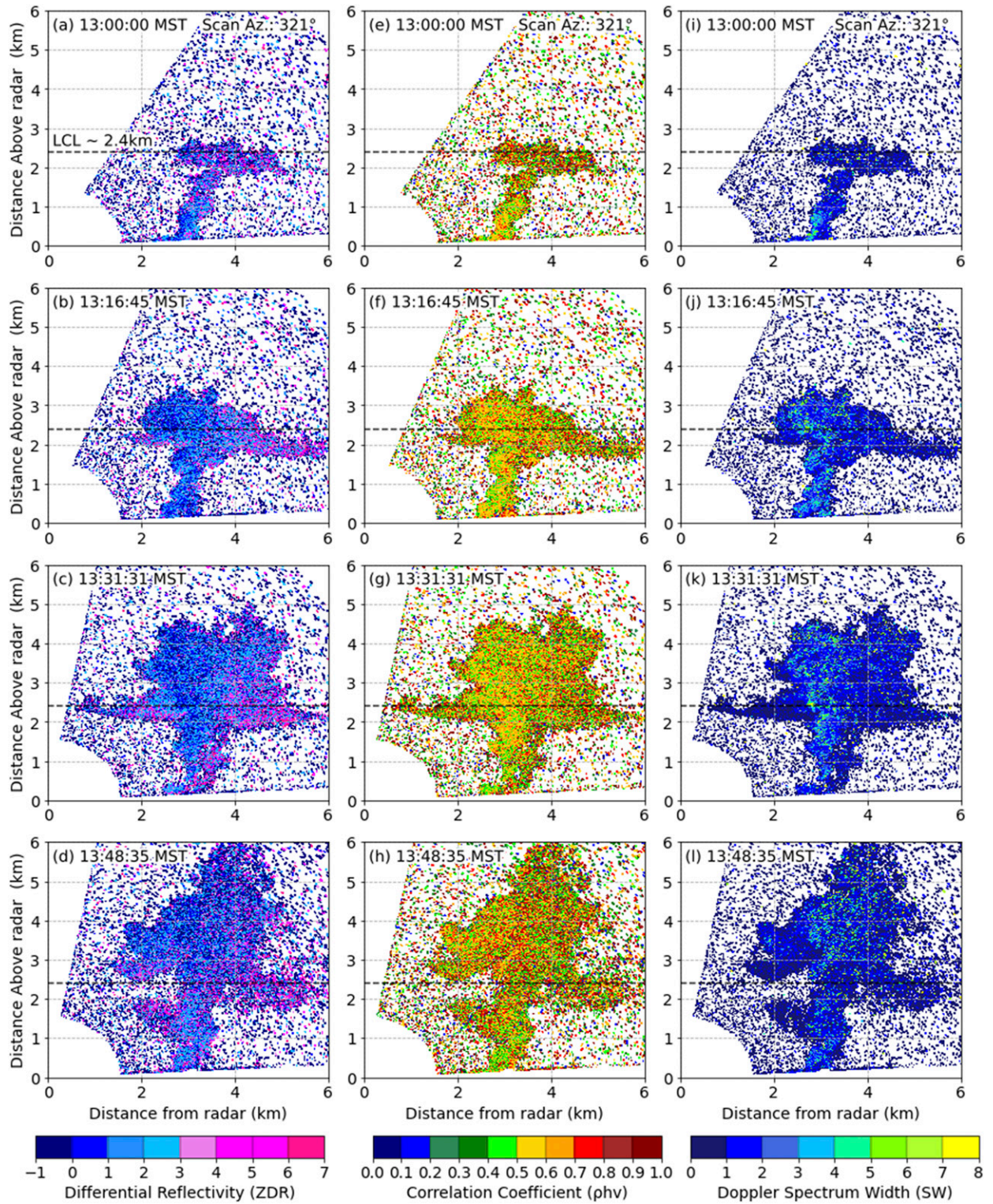
FIG. 8. Same RHI scan as Fig. 4 beginning at 1300 MST 7 Nov 2019, showing fields for (a)–(d) differential reflectivity (Z_{DR}), (e)–(h) copolar correlation coefficient (ρ_{hv}), and (i)–(l) Doppler spectrum width.
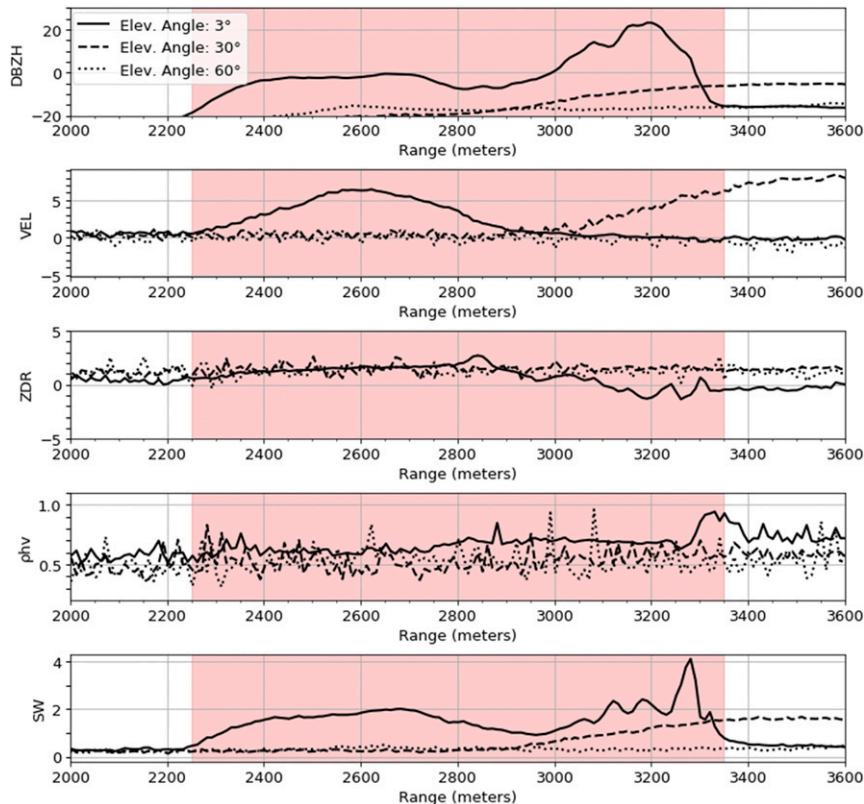
FIG. 9. Mean radar variables along the 3°, 30°, and 60° elevation beam, showing (top) horizontal radar reflectivity, (top middle) radial velocity, (middle) differential reflectivity, (bottom middle) copolar correlation coefficient, and (bottom) Doppler spectrum width. The red shading indicates the location where the beam was within the smoke plume.

the variables along the elevation beam provided a way to assess mean plume structure at various heights above the fire. Specifically, we examined elevation angles 3°, 30°, and 60°. For all variables, the lowest elevation angle depicts the greatest returns within the plume. Reflectivity, correlation coefficient, and Doppler spectrum width increased along the beam within in the plume. In contrast, average velocity and differential reflectivity decreased. These data indicate the most turbulent area of the plume is collocated with the regions of maximum reflectivity and correlation coefficient. Mean values along this elevation reveal that reflectivity values were between -2 and 20 dBZ and that radial velocities were 0–7 m s^{-1}; Z_{DR}, ρ_{HV}, and SW had mean values of 1dB, 0.6, and 2.5 m s^{-1}, respectively.

Elevation angles 30° and 60° represent the upper plume and illustrated different patterns than the lowest beam. Reflectivity values along these elevation angles were weak and values remained below 0 dBZ within the smoke plume. The average velocities along these beams have a mean of 0 m s^{-1}. Along the 30° beam, average velocities increased with distance along the radial beam ($\sim$3 km). The average differential reflectivity returns are of similar magnitude for all elevation angles; however, the higher elevation angles indicate a more strongly polarized signal with a mean value of 2 dB. In contrast, the

average correlation coefficients were lower at higher elevation angles, with an average value closer to 0.5. Mean Doppler spectrum width was less than 1 m s^{-1} and decreased with height. With the exception of the 30° beam, Doppler spectrum width decreased downwind of the plume.

Studies documenting mean polarimetric variables of wildfire smoke plumes have found similar values to that of the South Monroe prescribed burn. Melnikov et al. (2008) detailed mean Z_{DR} and ρ_{HV} to be 1.4 dB and 0.33, respectively, in a vertical cross section of a fire plume. Similarly, Jones and Christopher (2009) observed a mean Z_{DR} of 1.7 dB and ρ_{HV} of 0.49 in a low-elevation PPI scan. This study also recorded mean reflectivity values between -3 and 18 dBZ in the smoke plume, with few returns exceeding 20 dBZ. The most recent study that documented mean polarimetric variables of smoke plumes was that by Zrnić et al. (2020) in which a 10- and a 5-cm radar were used to observe three wildfires. Mean radar reflectivity values were of similar values to the ones in this study; however, mean Z_{DR} values were greater than 2 dB and mean ρ_{HV} were less than 0.5. Values from our study and those previously conducted are all of similar magnitude with the exception of correlation coefficient. Observations of correlation coefficients with KASPR were slightly higher than those documented in other studies, which is likely a result of the difference in wavelengths and

FIG. 10. KASPR radar signatures from the Briceburg wildfire beginning at 1328 PST 9 Oct 2019, showing fields for (a)–(d) horizontal reflectivity (dBZ_H) and (e)–(h) radial velocity (m s^{-1}).

beamwidths among radars. Additionally, in our observations several variables are shown to decrease on the leeward side of the plume. McCarthy et al. (2018) observed a decrease in Doppler spectrum width in the leeward zone of a smoke plume, which is also evident in our observations.

6. Briceburg wildfire observations

The Briceburg wildfire ignited on the afternoon of 6 October 2019 in Mariposa County, California, at approximately 37.605°N, 119.966°W (Cal Fire 2019a). KASPR was deployed on 9 October to observe and collect data on the Briceburg smoke plume. Dry and windy conditions were forecast to persist throughout the day, providing conditions favorable for rapid fire growth. On this day, the fire burned over 1000 acres and produced a visible pyrocumulus from satellite imagery. Complex terrain and major road closings in the area made it difficult to obtain a radar site close to the fire. The chosen site was located on a ridge approximately 13 km southwest of the fire at 37.535°N, 120.030°W. KASPR operated RHI scans with a targeted scan rate of $1°$ s^{-1} through elevation angles from 0.05° to 11.65° (Table 2). This analysis focuses on a period during which the plume grew vertically and reached a height of 3 km AGL.

Radar observations from Briceburg wildfire

Figures 10a–h illustrates radar reflectivity and velocity observations of the Briceburg wildfire beginning at 1325 PST. Radar reflectivity measured from −14 to 6 dBZ within the plume, with the highest values located near the plume base. Cores of reflectivity > -4 dBZ propagated vertically through the entire depth of the plume (Fig. 10a) and advected downwind with the ambient flow (Fig. 10b). At 1340:26 PST (Fig. 10c), a coherent reflectivity core was observed to extend from the surface to a height of ~1.2 km AGL. This plume core was ~250–500 m in width and indicates a region where a coherent and continuous high-reflectivity core representing pyrometeors extended through the height of the plume. This observed structure suggests that pyrometeors and debris are advected vertically through the plume and ejected out the top and downwind of the plume updraft core. Outside the plume updraft reflectivity cores, the plume is characterized by weak returns, which is likely a result of either the scanning range or more dispersed pyrometeors. Radial velocity returns indicated the plume particles were traveling away from the radar at 3–12 m s^{-1}. The first scan (Fig. 10e) depicts contrasting inbound and outbound velocities below 0.5 km AGL, indicating converging flow at the plume base. An area of weak inbound velocities (~3 m s^{-1}) is observed in all scans from 0.5 to 1.5 km AGL, illustrating plume overturning and entrainment on the upwind and downwind edges of the plume.

Observations of the Briceburg wildfire illustrate coarser range resolution measurements of reflectivity and radial velocity. Operating in polarimetric pulse pair mode examines the polarimetric parameters at the lowest sensitivity among the settings, which further lowered the resolution of our scans. Because of these limiting factors, observations were not as detailed as the others shown in this study. However, these data
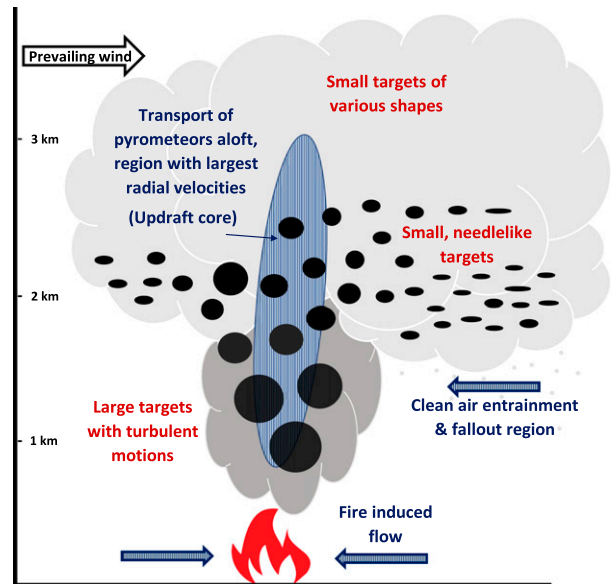

FIG. 11. Conceptual diagram detailing the observed dual-polarimetric and kinematic structures.

indicate that, even at long-range, KASPR observations of wildfire smoke plumes can provide information on plume dynamics and evolution. This case study highlights how narrow reflectivity cores propagate through the entire depth of the plume and eject smoke and pyrometeors out the top and downwind.

7. Discussion

Through the analysis of radar reflectivity, radial velocity, and polarimetric properties, insight into Ka-band radar specific signatures of smoke plumes is shown. A conceptual diagram was created to show an overview of the findings from this study highlighting the dual-polarization observations (Fig. 11). Specifically, this diagram details the areas of turbulent motions, the various shapes of targets within the plume, and the overall transport of pyrometeors found in our observations. Within this study, distributions of radar reflectivity were similar across all deployments, revealing values between −15 and 20 dBZ within the plume and some reflectivity cores exceeding this upper limit. Areas of maxima reflectivity were associated with maxima in radial velocity and Doppler spectrum width and were located near the base of the plume and updraft core zone for all plumes sampled. Radial velocity structures revealed converging flow into the base of the plume and diverging flow aloft. Clean-air entrainment was also observed in the radial velocity signatures from the Kincade D1 and D2 and South Monroe deployments.

The observed polarimetric parameters were similar to those of previous studies using radar to investigate polarimetric properties of wildfire plumes (Melnikov et al. 2008; Jones and Christopher 2009; McCarthy et al. 2018; Zrnić et al. 2020). Positive values of Z_{DR} paired with low ρ_{HV} indicate wildfire targets are of various shapes and sizes in each sample volume.

Positive Z_{DR} values were associated with low reflectivity values and remained outside the primary updraft location, with maximum values near 6 dB. Positive Z_{DR} values indicate the needle-like appearance of ash and smoke that has been concluded from previous studies (Melnikov et al. 2008; Jones and Christopher 2009). Relatively low Z_{DR} values inside the primary updraft location were likely a result of turbulent motions and shear. Correlation coefficient values remained below 0.8 for in plume observations, with the lowest values (~0.3) located near plume base, revealing that a wide array of particle shapes and motions was present. Furthermore, K_{DP} values were calculated for the South Monroe plume only (not shown) and indicated that K_{DP} was small, ($<1.0°$ km^{-1}) throughout the plume.

8. Conclusions

Dual polarimetric Ka-band radar measurements of two wildfires and one prescribed crown fire were used to observe the fine-scale kinematics and dual polarimetric properties of smoke plumes. This study highlights the advantages of utilizing a portable, millimeter-wavelength radar for monitoring and investigating wildfire plume dynamics and microphysics. The results from this study highlight the high-temporal-and-spatial-resolution observations of wildfire smoke plumes obtained from millimeter-wavelength radars. Utilizing compact and mobile radars allows for continuous, close-range and highly resolved observations of wildfire smoke plumes that the operational NEXRAD WSR-88D network cannot always provide. In addition, millimeter-wavelength radars are more ideally suited for studying small pyrometeors lofted from wildfires than the operational 10-cm weather radars. Further investigation into the fine-scale kinematics and microphysical properties of wildfire smoke plumes will aid in the development and validation of better predictive tools for wildfire behavior by incorporating these types of observations into next-generation spotting and transport models.

REFERENCES

Adams, R. J., W. F. Perger, W. I. Rose, and A. Kostinski, 1996: Measurements of the complex dielectric constant of volcanic ash from 4 to 9 GHz. *J. Geophys. Res.*, **101**, 8175–8185, https://doi.org/10.1029/96JB00193.

Banta, R. M., L. D. Olivier, E. T. Holloway, R. A. Kropfli, B. W. Bartram, R. E. Cupp, and M. J. Post, 1992: Smoke-column observations from two forest fires using Doppler lidar and Doppler radar. *J. Appl. Meteor.*, **31**, 1328–1349, https://doi.org/10.1175/1520-0450(1992)031<1328:SCOFTF>2.0.CO;2.

Baum, T. C., L. Thompson, and K. Ghorbani, 2015: The nature of fire ash particles: Microwave material properties, dynamic behavior, and temperature correlation. *IEEE J. Sel. Top. Appl. Earth Obs. Remote Sens.*, **8**, 480–492, https://doi.org/10.1109/JSTARS.2014.2386394.

Bluestein, H. B., 1999: A history of severe-storm-intercept field programs. *Wea. Forecasting*, **14**, 558–577, https://doi.org/10.1175/1520-0434(1999)014<0558:AHOSSI>2.0.CO;2.

Bryan, S., A. Clarke, L. Vanderkluysen, C. Groppi, S. Paine, and D. W. Bliss, 2017: Measuring water vapor and ash in volcanic eruptions with a millimeter-wave radar/imager. *IEEE Trans. Geosci. Remote Sens.*, **55**, 3177–3185, https://doi.org/10.1109/TGRS.2017.2663381.

Cal Fire, 2019a: Incidents-Briceburg Fire. Accessed 20 March 2019, https://fire.ca.gov/incidents/2019/10/6/briceburg-fire/.

——, 2019b: Incidents-Kincade Fire. Accessed 23 March 2019, https://www.fire.ca.gov/incidents/2019/10/23/kincade-fire/.

——, 2019c: Incidents-Camp Fire. Accessed 1 September 20, https://www.fire.ca.gov/incidents/2018/11/8/camp-fire/.

Charland, A. M., and C. B. Clements, 2013: Kinematic structure of a wildland fire plume observed by Doppler lidar. *J. Geophys. Res. Atmos.*, **118**, 3200–3212, https://doi.org/10.1002/jgrd.50308.

Clements, C. B., and A. J. Oliphant, 2014: The California State University Mobile Atmospheric Profiling System: A facility for research and education in boundary layer meteorology. *Bull. Amer. Meteor. Soc.*, **95**, 1713–1724, https://doi.org/10.1175/BAMS-D-13-00179.1.

——, and Coauthors, 2007: Observing the dynamics of wildland grass fires: FireFlux—A field validation experiment. *Bull. Amer. Meteor. Soc.*, **88**, 1369–1382, https://doi.org/10.1175/BAMS-88-9-1369.

——, and Coauthors, 2015: Fire weather conditions and fire–atmosphere interactions observed during low-intensity prescribed fires—RxCADRE 2012. *Int. J. Wildland Fire*, **25**, 90–101, https://doi.org/10.1071/WF14173.

——, N. P. Lareau, D. E. Kingsmill, C. L. Bowers, C. P. Camacho, R. Bagley and B. Davis, 2018: The Rapid Deployments to Wildfires Experiment (RaDFIRE): Observations from the fire zone. *Bull. Amer. Meteor. Soc.*, **99**, 2539–2559, https://doi.org/10.1175/BAMS-D-17-0230.1.

Cruz, M. G., A. L. Sullivan, J. S. Gould, N. C. Sims, A. J. Bannister, J. J. Hollis, and R. J. Hurley, 2012: Anatomy of a catastrophic wildfire: The Black Saturday Kilmore East fire in Victoria, Australia. *For. Ecol. Manage.*, **284**, 269–285, https://doi.org/10.1016/j.foreco.2012.02.035.

Dempsey, F., 2013: Forest fire effects on air quality in Ontario: Evaluation of several recent examples. *Bull. Amer. Meteor. Soc.*, **94**, 1059–1064, https://doi.org/10.1175/BAMS-D-11-00202.1.

Fromm, M., A. Tupper, D. Rosenfeld, R. Servranckx, and R. McRae, 2006: Violent pyro-convective storm devastates Australia's capital and pollutes the stratosphere. *Geophys. Res. Lett.*, **33**, L05815, https://doi.org/10.1029/2005GL025161.

——, R. H. D. McRae, J. J. Sharples, and G. P. Kablick III, 2012: Pyrocumulonimbus pair in Wollemi and Blue Mountains National Parks, 22 November 2006. *Aust. Meteor. Oceanogr. J.*, **62**, 117–126, https://doi.org/10.22499/2.6203.001.

Helmus, J. J., and S. M. Collis, 2016: The Python ARM Radar Toolkit (Py-ART), a library for working with weather radar

data in the Python programming language. *J. Open Res. Software*, **4**, e25, https://doi.org/10.5334/jors.119.

Jones, T. A., and S. A. Christopher, 2009: Injection heights of biomass burning debris estimated from WSR-88D radar observations. *IEEE Trans. Geosci. Remote Sens.*, **47**, 2599–2605, https://doi.org/10.1109/TGRS.2009.2014225.

——, and ——, 2010: Satellite and radar remote sensing of southern plains grass fires: A case study. *J. Appl. Meteor. Climatol.*, **49**, 2133–2146, https://doi.org/10.1175/2010JAMC2472.1.

——, ——, and W. Petersen, 2009: Dual-polarization radar characteristics of an apartment fire. *J. Atmos. Oceanic Technol.*, **26**, 2257–2269, https://doi.org/10.1175/2009JTECHA1290.1.

Koo, E., P. J. Pagni, D. R. Weise, and J. P. Woycheese, 2010: Firebrands and spotting ignition in large-scale fires. *Int. J. Wildland Fire*, **19**, 818–843, https://doi.org/10.1071/WF07119.

Lang, T. J., S. A. Rutledge, B. Dolan, P. Krehbiel, W. Rison, and D. T. Lindsey, 2014: Lightning in wildfire smoke plumes observed in Colorado during summer 2012. *Mon. Wea. Rev.*, **142**, 489–507, https://doi.org/10.1175/MWR-D-13-00184.1.

Lareau, N. P., and C. B. Clements, 2015: Cold smoke: Smoke-induced density currents cause unexpected smoke transport near large wildfires. *Atmos. Chem. Phys.*, **15**, 11 513–11 520, https://doi.org/10.5194/acp-15-11513-2015.

——, and ——, 2016: Environmental controls on pyrocumulus and pyrocumulonimbus initiation and development. *Atmos. Chem. Phys.*, **16**, 4005–4022, https://doi.org/10.5194/acp-16-4005-2016.

——, and ——, 2017: The mean and turbulent properties of a wildfire convective plume. *J. Appl. Meteor. Climatol.*, **56**, 2289–2299, https://doi.org/10.1175/JAMC-D-16-0384.1.

——, N. J. Nauslar, and J. T. Abatzoglou, 2018: The Carr Fire vortex: A case of pyrotornadogenesis? *Geophys. Res. Lett.*, **45**, 13 107–13 115, https://doi.org/10.1029/2018GL080667.

LaRoche, K. T., and T. J. Lang, 2017: Observations of ash, ice, and lightning within pyrocumulus clouds using polarimetric NEXRAD radars and the national lightning detection network. *Mon. Wea. Rev.*, **145**, 4899–4910, https://doi.org/10.1175/MWR-D-17-0253.1.

Maesaka, T., K. Iwanami, and M. Maki, 2012: Non-negative K_{DP} estimation by monotone increasing Φ_{DP} assumption below melting layer. *Seventh European Conf. on Radar Meteorology and Hydrology* (*ERAD 2012*), Toulouse, France, Météo-France, http://www.meteo.fr/cic/meetings/2012/ERAD/extended_abs/QPE_233_ext_abs.pdf.

McCarthy, N., H. McGowan, A. Guyot, and A. Dowdy, 2018: Mobile X-Pol radar: A new tool for investigating pyroconvection and associated wildfire meteorology. *Bull. Amer. Meteor. Soc.*, **99**, 1177–1195, https://doi.org/10.1175/BAMS-D-16-0118.1.

——, A. Guyot, A. Dowdy, and H. McGowan, 2019: Wildfire and weather radar: A review. *J. Geophys. Res. Atmos.*, **124**, 266–286, https://doi.org/10.1029/2018JD029285.

McRae, R., J. J. Sharples, and M. Fromm, 2015: Linking local wildfire dynamics to pyroCb development. *Nat. Hazards Earth Syst. Sci.*, **15**, 417–428, https://doi.org/10.5194/nhess-15-417-2015.

Melnikov, V. M., D. S. Zrnić, R. M. Rabin, and P. Zhang, 2008: Radar polarimetric signatures of fire plumes in Oklahoma. *Geophys. Res. Lett.*, **35**, L14815, https://doi.org/10.1029/2008GL034311.

——, ——, and ——, 2009: Polarimetric radar properties of smoke plumes: A model. *J. Geophys. Res.*, **114**, D21204, https://doi.org/10.1029/2009JD012647.

Penner, J. E., R. E. Dickinson, and C. S. O'Neill, 1992: Effects of aerosol from biomass burning on the global radiation budget. Science, 256, 1432–1434, https://doi.org/10.1126/science.256.5062.1432.

Price, O. E., B. Horsey, and N. Jiang, 2016: Local and regional smoke impacts from prescribed fires. *Nat. Hazards Earth Syst. Sci.*, **16**, 2247–2257, https://doi.org/10.5194/nhess-16-2247-2016.

Prichard, S. J., and Coauthors, 2019: The Fire and Smoke Model Evaluation Experiment—A plan for integrated, large fire-atmosphere field campaigns. *Atmosphere*, **10**, 66, https://doi.org/10.3390/atmos10020066.

ProSensing, 2019: Ka-band Scanning Polarimetric Radar (KASPR). Accessed 1 April 2019, https://www.prosensing.com/crb-product/ka-band-scanning-polarimetric-radar-kaspr/.

Rauber, R. M., and S. W. Nesbitt, 2018: *Radar Meteorology: A First Course*. John Wiley and Sons, 461 pp.

Rodriguez, B., N. P. Lareau, D. E. Kingsmill, and C. B. Clements, 2020: Extreme pyroconvective updrafts during a megafire. *Geophys. Res. Lett.*, **47**, e2020GL089001, https://doi.org/10.1029/2020GL089001.

Schneebeli, M., J. Grazioli, and A. Berne, 2014: Improved estimation of the specific differential phase shift using a compilation of Kalman filter ensembles. *IEEE Trans. Geosci. Remote Sens.*, **52**, 5137–5149, https://doi.org/10.1109/TGRS.2013.2287017.

Vulpiani, G., M. Montopoli, L. D. Passeri, A. G. Gioia, P. Giordano, and F. S. Marzano, 2012: On the use of dual-polarized C-band radar for operational rainfall retrieval in mountainous areas. *J. Appl. Meteor. Climatol.*, **51**, 405–425, https://doi.org/10.1175/JAMC-D-10-05024.1.

Zrnić, D., P. Zhang, V. Melnikov, and D. Mirkovic, 2020: Of fire and smoke plumes, polarimetric radar characteristics. *Atmosphere*, **11**, 363, https://doi.org/10.3390/atmos11040363.